Zero Cu valence and superconductivity in high-quality $Cu_xBi_2Se_3$ crystal

Shih-Hsun Yu,[1,2,3] Tsu Lien Hung,[3] Min-Nan Ou [3,*] Mitch M. C. Chou,[1,2,†] and Yang-Yuan Chen[3,‡]

[1]*Center of Crystal Research, Department of Materials and Optoelectronic Science,*
National Sun Yat-Sen University, Kaohsiung 80424, Taiwan, R.O.C.
[2]*NSC Taiwan Consortium of Emergent Crystalline Materials (TCECM), Kaohsiung, Taiwan, R.O.C.*
[3]*Institute of Physics, Academia Sinica, Taipei 11529, Taiwan, R.O.C.*

In this work, the role of Cu dopants in the development of superconductivity in Bi_2Se_3 is investigated. A series of $Cu_xBi_2Se_3$ ($x = 0$–0.3) crystals is grown using the Bridgman method and electrochemical techniques. Based on the observable lattice increases along the c axis, the existence of Cu atoms intercalated in the van der Waals (vdW) gaps in Bi_2Se_3 is verified by x-ray diffraction, scanning electron microsopy–energy dispersive spectroscopy, and transmission electron microscopy analysis. Furthermore, the chemical state of the Cu is found to be zero valence by characterization of the x-ray photoelectron and Auger electron spectra. The absence of Cu^{1+} and Cu^{2+} in the electron energy-loss spectroscopy near-edge fine structure is confirmed as well. Meanwhile, our Raman data also show the same result: the intercalation of Cu in the vdW gap which weakens the binding of the quintuple layers in the $Cu_{0.1}Bi_2Se_3$ crystal. The electric resistance and magnetic susceptibility show a superconducting transition near 3–3.4 K in the series of Cu-doped Bi_2Se_3. A sharp superconducting transition with the highest value of $T_C = 3.4\,K$ and the largest magnetic shielding fraction of 84% is observed in the optimized 10% Cu-doped Bi_2Se_3. These results imply that the formation of superconducting quasiparticles is not related to the charge transfer of Cu, but is supported by the internal stress of Cu intercalated in the van der Waals gap. The superconducting transition observed in the specific heat implies that the superconductivity in $Cu_xBi_2Se_3$ is unconventional.

I. INTRODUCTION

Substantial research efforts have gone into creating a surface interface between a TI with a robust gap and an ordinary s-wave superconductor [1,2]. Three-dimensional (3D) topological insulator systems with a single Dirac cone such as Bi_2Se_3, Bi_2Te_3, and Sb_2Te_3 were predicted by the theoretical band structure calculation [3,4] and subsequently found by experimental work. These three compounds, Bi_2Se_3, Bi_2Te_3, and Sb_2Te_3, have attracted great interest due to the possibility of finding a superconducting (SC) state on the surface of or interfaces involving these systems. Currently, Bi_2Se_3 has a known topological surface state and a clear Dirac cone, which have been mapped out by angle-resolved photoemission spectroscopy (ARPES) [5]. Meanwhile, Cu-doped Bi_2Se_3 has been found to be an odd-parity superconductor with a unique rotational symmetry breaking (or nematic) state, believed [6] to be a characteristic of a topological superconducting state capable of hosting Majorana bound states (MBSs) [7,8].

The lattice structure of Bi_2Se_3 is classified as a rhombohedral structure of space group $D_{3d}^5(R\bar{3}m)$. Its hexagonal plane is composed of Bi and Se atoms, closely stacked along the c axis with a repeated order of Se (1) – Bi – Se (2) – Bi – Se (1) every five atomic layers, which naturally forms

quintuple layers (QLs). Various synthesis techniques [9–13] are employed to intercalate the dopant atom into the van der Waals (vdW) gap without creating dramatic deformation of the host lattice structure. Since the space gap between two neighboring quintuple layers is around 2.4–2.6 Å [14], it allows the insertion of atoms ($d_{Cu} \sim 1.8$ Å) [15] by a room temperature intercalation process.

Significant SC behavior was first discovered by Hor *et al.* in Cu intercalated Bi_2Se_3 specimens prepared by a mixed melt-growth technique. However, the specimens fabricated by the melt-growth method show superconductivity only in some cases [11]. Kriener *et al.* [12] further utilized a much better controlled electrochemical (EC) technique to insert Cu into the vdW gaps of Bi_2Se_3 with a high superconducting shielding fraction. To date, Mn [16], Tl [17], Nb [18,19], Ca [20], Cd [21], and Sr [22–27] elements have been successfully chemically doped into Bi-Te-Se based compounds. However, only the Cu-doped [6–8], Tl-doped [17], Nb-doped [18,19], and Sr-doped [25] Bi-Te-Se based compounds show prominent superconductivity, with Cu-, Sr-, and Nb-doped Bi_2Se_3 demonstrating a nematic superconducting state. Meanwhile, relevant theoretical simulations [28,29] regarding nematic and chiral superconductivity have been carried out to facilitate the understanding of such exotic phenomena. These discoveries provide the possibility that $Cu_xBi_2Se_3$ is not only a topological superconductor material but also a potential candidate for realizing the MBS. However, even though $Cu_xBi_2Se_3$ has been intensively studied, the role of Cu in the formation of SC quasiparticles in $Cu_xBi_2Se_3$ is still an ambiguous issue.

*oumn@gate.sinica.edu.tw
†mitch@faculty.nsysu.edu.tw
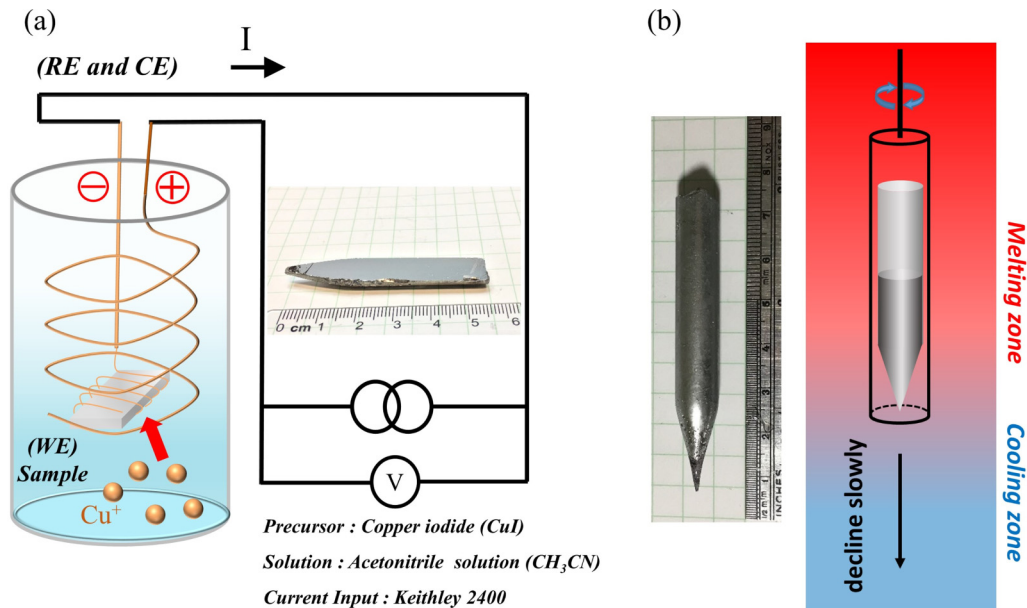‡cheny2@phys.sinica.edu.tw

FIG. 1. Schematic diagram of the synthesis of single-crystal Bi_2Se_3 showing the (a) homemade electrochemical setup. The inset shows a pristine Bi_2Se_3 with a lustrous cleavage plane and mirrorlike surface; (b) a Bi_2Se_3 single crystal with a length of 6.5 cm and a diameter of 1 cm grown by the vertical Bridgman furnace method.

In order to ascertain the locations of Cu and its valence state in a $Cu_xBi_2Se_3$ single crystal, spectroscopic tools such as the x-ray photoelectron spectra (XPS), Auger electron spectra (AES), and electron energy-loss spectroscopy (EELS) were applied to investigate the role of Cu in the formation of superconductivity in $Cu_xBi_2Se_3$. To avoid the formation of Cu-Bi and Cu-Se chemical bonds in the quintuple layers, $Cu_xBi_2Se_3$ was fabricated by intercalating Cu into the Bi_2Se_3 quintuple layers using EC deposition. The lattice structure, transport, magnetic, and specific heat properties of the pristine and Cu-doped Bi_2Se_3 crystals were characterized by x-ray diffraction, electrical resistivity, magnetic susceptibility, and specific heat using a physical property measurement system (PPMS), magnetic property measurement system (MPMS), and home-made calorimetry, respectively. The superconducting transition and magnetic shielding fractions of the Meissner effect were clearly observable. This work describes the details of site occupation and the valence of Cu in the formation of superconductivity in Cu-doped Bi_2Se_3. Moreover, the data of specific heat observed in the SC transition implies that the superconductivity in $Cu_xBi_2Se_3$ is unconventional in character.

II. EXPERIMENTAL DETAILS

A. Sample fabrication and characterization

There are numerous methods [6–8,12,30] that have been successfully used for the intercalation of Cu into the Bi_2Se_3 host material, including the melt growth following the electrochemical (EC) technique introduced by Kriener *et al.* [12]. However, in the present work, to improve the quality of pristine Bi_2Se_3, the melt crystal growth method has been replaced by the Bridgman method. Therefore, we employed a two-step process to synthesize a series of high-quality $Cu_xBi_2Se_3$ ($x = 0$–0.3) crystals. First, Bi_2Se_3 crystals were grown from a Bi_2Se_3 melt using the Bridgman method (BM)

[Fig. 1(b)] followed by EC deposition to insert Cu into the Bi_2Se_3 crystals [Fig. 1(a)]. To grow Bi_2Se_3 crystals, high-purity elements of Bi (99.999%) and Se (99.999%) were well ground and mixed using a stoichiometric ratio of 2:3, then sealed in an evacuated quartz ampoule (6.5 cm in length and 1.2 cm in diameter) under a vacuum of $\sim 3 \times 10^{-5}$ Torr. The sealed quartz ampoule was then annealed at 850 °C for 48 h followed by slow cooling at a rate 5 mm/h until cold, and then postannealed at 550 °C for 48 h. The high quality of the Bi_2Se_3 single crystals is revealed by the lustrous mirrorlike surface [see the inset to Fig. 1(a)]. In the second step of EC deposition, a sample piece (4 mm in length, 0.1 mm in thickness, and 2 mm in width) was cleaved from the Bi_2Se_3 crystal along the vdW gap which was then cut into a rectangular shape. A bare copper wire was wound around the sample to form the working electrode (WE). An oxygen-free copper belt (2 mm in width) functioned as the counter electrode (CE) and reference electrode (RE) for immersion in a CuI-acetonitrile solution [Fig. 1(a)]. A constant current of 100 μA was applied to reduce the Cu ions for the realization of Cu intercalation in a nitrogen flow environment at room temperature. No noticeable crack or deformation was observed after the redox process. The Cu intercalated Bi_2Se_3 crystals were annealed at 550 °C in vacuum for 2 h followed by quenching in water. They could be easily cleaved along the basal plane. A series of $Cu_xBi_2Se_3$ ($x = 0$, 0.08, 0.1, 0.15, 0.2, 0.3) crystals was prepared with the same procedure. The nominal x content of Cu was defined by taking the corresponding molar ratio of the reduced Cu following the formula $xCu^+ + xe^- \rightarrow xCu$. The electron number x was calculated from the working current and total reduction time. To reduce the influence of oxygen on our air-sensitive sample, the electrochemical experiment was performed in a nitrogen flow box. After that, all specimens were sealed in quartz tubes in high vacuum; all measurements were performed in high vacuum as well.
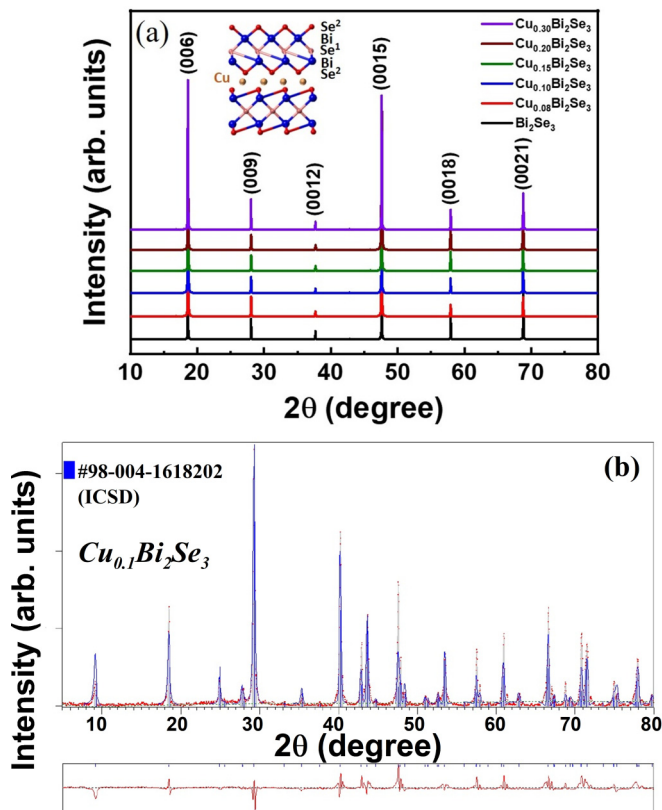
FIG. 2. (a) The x-ray diffraction patterns of $Cu_xBi_2Se_3$ ($x = 0.08–0.3$) at room temperature, revealing the (00l) preferred orientation. The inset displays the schematic figure with Cu in its intercalated position; (b) powder x-ray diffraction pattern and Rietveld-fitted result of $Cu_{0.1}Bi_2Se_3$.

FIG. 3. (a)–(d) SEM images of pristine Bi_2Se_3 under various magnification and $Cu_{0.1}Bi_2Se_3$ crystal: (a), (b) the layered structures in both Bi_2Se_3 and $Cu_{0.1}Bi_2Se_3$ (indicated by the white arrows) are clearly revealed by SEM with the incident electron beam along the c axis.

The crystal structure and lattice constant of Bi_2Se_3 and $Cu_xBi_2Se_3$ ($x = 0–0.3$) crystals were investigated by x-ray diffraction. Figure 2(a) shows the characteristic planes of (00l) by triple-axis XRD [Materials Research Diffractometers (MRD) XL] on the cleavage plane of the samples in Fig. 1(a), confirming the single-crystalline nature of the specimens. The powder x-ray diffraction (PXRD) (PANalytical X'pert³ Powder) in Fig. 2(b) indicates a rhombohedral crystal structure, which was in good agreement with earlier literature [31–33]. The lattice constants of the pristine and $Cu_{0.1}Bi_2Se_3$ crystals determined by the Rietveld refinement of X'pert HIGHSCORE PLUS software are shown in Table I. The pattern was refined to the Bragg peak positions of the Bi_2Se_3 crystal with a rhombohedral structure and corroborated by the Inorganic Crystal Structure Database (ICSD) #98-004-8202. Moreover, the characteristic peak of Cu in the powder
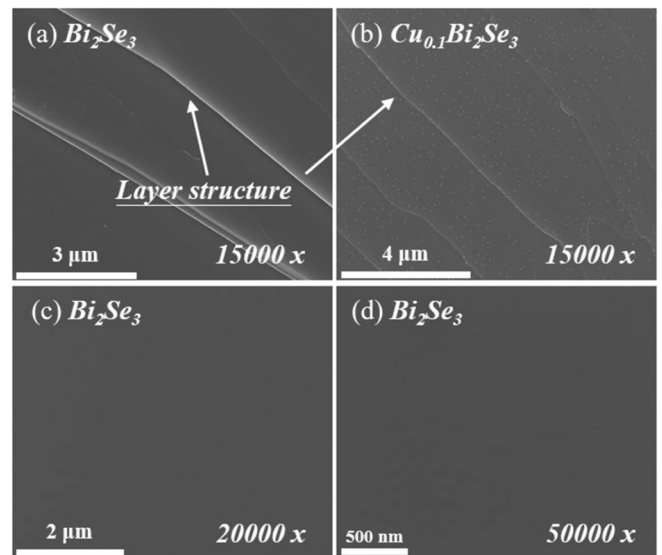
x-ray diffraction pattern cannot be seen in the minor Cu intercalation [34]. For the $Cu_{0.1}Bi_2Se_3$ crystal, a noticeable increase (∼0.6%) in the c axis but a barely observable one in the a axis (∼0.1%) supports the interpretation that Cu was intercalated in the vdW gap. Since the ion radii of Cu^+ (0.91 Å) and Cu^{2+} (0.87 Å) are much smaller than that of Bi^{3+} (1.19 Å), if Cu is substituted for Bi, the lattice constants of a and b should be reduced; however, there was almost no change (∼0.1%) in lattice constants a and b, implying that there was no or very little Cu substitution for Bi. Moreover, if the Se is replaced by Cu atoms through substitution or an interstitial interaction, the second phase will be found to create the structural deformation, respectively. Lastly, the optical analysis results (discussed later) support the conclusion that the Cu atoms are not bound with Se atoms.

Scanning electron microscopy (SEM) (FEI NOVA-600) and energy dispersive spectroscopy (EDS) (OXFORD Ultim Max) were employed for the investigation of the micromorphology and chemical composition of $Cu_xBi_2Se_3$ crystals, respectively. The SEM images in Figs. 3(a) and 3(b) present the layered structure of Bi_2Se_3 and $Cu_{0.1}Bi_2Se_3$ crystals, respectively. In the SEM images of $Cu_{0.1}Bi_2Se_3$, the Cu atoms uniformly distributed throughout the crystal are represented by small white spots [Fig. 3(b)]. There were no observable Bi clusters in our crystals in contrast to the samples described

TABLE I. The lattice parameters of Bi_2Se_3 and $Cu_{0.1}Bi_2Se_3$.

Sample label	Lattice parameter		
	Lattice a	Lattice c	Cell volume
Bi_2Se_3 [51]	4.14 ± 0.01 Å	28.636 Å ± 0.04 Å	425.67
Bi_2Se_3	4.139 Å	28.596 Å	424.25
$Cu_{0.1}Bi_2Se_3$	4.135 Å	28.762 Å	425.89

TABLE II. The SEM-EDS elemental composition for Bi_2Se_3 and $Cu_{0.1}Bi_2Se_3$ crystals. The notation "avg." means the average value of five sampled spots 2 μm in size from Fig. 3.

| Sample label | Composition | | | |
	Cu (at. %)	Bi (at. %)	Se (at. %)	Calculated composition
SEM-Bi_2Se_3 (avg.)	0	41.1 ± 0.7	58.9 ± 0.7	$Bi_{2.05}Se_{2.95}$
SEM-$Cu_{0.1}Bi_2Se_3$ (avg.)	2.4 ± 0.5	38.8 ± 0.5	58.8 ± 0.4	$Cu_{0.12}Bi_{1.94}Se_{2.94}$

by Huang *et al.* [35]. The stoichiometry of the Bi_2Se_3 and $Cu_{0.1}Bi_2Se_3$ was determined by SEM-EDS analysis (see Table II). The calculated composition for the bulk specimen Bi_2Se_3 was $Bi_{2.05}Se_{2.95}$ which is quite reasonable considering the ~5% resolution of the SEM-EDS. The SEM-EDS analysis of the bulk $Cu_{0.1}Bi_2Se_3$ with a sampling spot of $100 \times 100 \mu m^2$ shows a calculated composition of $Cu_{0.12}Bi_{1.94}Se_{2.94}$, a result which is quite consistent with the nominal value.

Bi_2Se_3 and $Cu_{0.1}Bi_2Se_3$ crystal foil was cut from the bulk material using a triple-axis FIB machine (Hitachi NX2000) for high-resolution transmission electron microscopy (HRTEM, JEOL JEM-2100F), as shown in the insets to Figs. 4(a) and 4(d), respectively. The interplanar spacing was 0.26 nm of {100} for Bi_2Se_3 and 0.385 nm of {11$\bar{2}$0} for $Cu_{0.1}Bi_2Se_3$ as shown in Figs. 4(b) and 4(d), respectively, indicating the nearly faultless lattice structures. Figure 4(c) displays an image of the Bi_2Se_3 crystal along with the fast Fourier transforms (FFTs), demonstrating the single-crystal characteristics of the specimen. As can be seen in Fig. 4(e),

the selected area electron diffraction (SAED) pattern of our $Cu_{0.1}Bi_2Se_3$ specimen exhibits sharp ordered spots without a trace of the polycrystalline or superlattice structure, which has been reported in earlier studies [36–38]. Meanwhile, the SAED pattern also shows a well indexed hexagonal structure and indicates that the layer structure grew in the [0001] direction. Furthermore, after the copper intercalation process, the grown $Cu_{0.1}Bi_2Se_3$ still preserves high-quality crystallinity, as revealed by the fast Fourier transform (FFT) results shown in Fig. 4(f).

The results of scanning transmission electron microscopic (STEM, JEOL JEM-2100F) analysis of the surface of a specimen cut by a triple-axis focused ion beam is shown in Fig. 5. A couple of Cu clusters were observed in the specimen [the white spots circled in Fig 5(a); chemical element of Cu was identified by EDS]. The TEM energy dispersive line scan profile and elemental mapping images are plotted in the upper right corner of Fig. 5(a) and Figs. 5(b)–5(d), respectively. The results indicate that the Bi, Se, and Cu are uniformly distributed throughout the bulk material. As reported by the
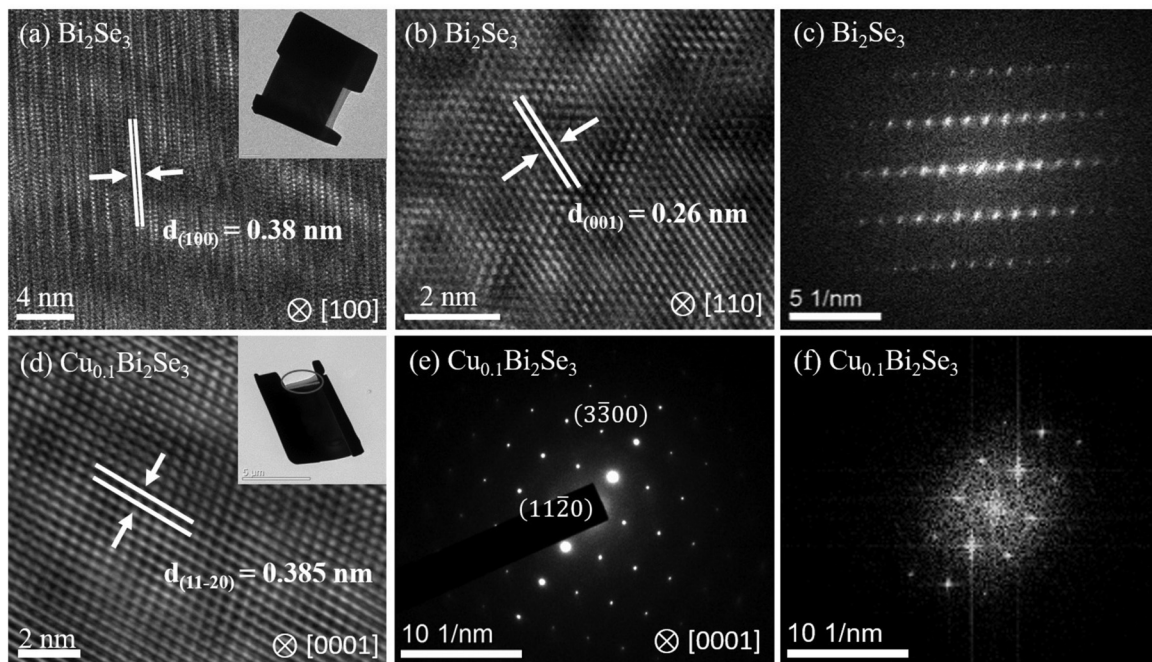

FIG. 4. (a), (d) High-resolution TEM images of Bi_2Se_3 and $Cu_{0.1}Bi_2Se_3$ single crystals; the insets display the surface of the TEM foil with size of 4 um × 4.6 um, 90 nm in thickness, cut by Ga ion irradiation via FIB (Hitachi NX2000), respectively: (a), (b) show that interplane $d_{(100)} = 0.38$ nm and $d_{(001)} = 0.26$ observed from different incident beam directions with no observable structural distortion; (c) image of the Bi_2Se_3 crystal along with the fast Fourier transform (FFT) results, with an aberration corrected JEOL JEM-2100F at 200 keV, demonstrating single-crystal characteristics; (d) HRTEM image of $Cu_{0.1}Bi_2Se_3$ with $d_{(11-20)} = 0.385$ nm; (e) SAED pattern of $Cu_{0.1}Bi_2Se_3$ from the circled area in the inset to (d), taken along the [0001] projection; (f) fast Fourier transform (FFT) results for (d) demonstrating no second phase $Cu_{0.1}Bi_2Se_3$.
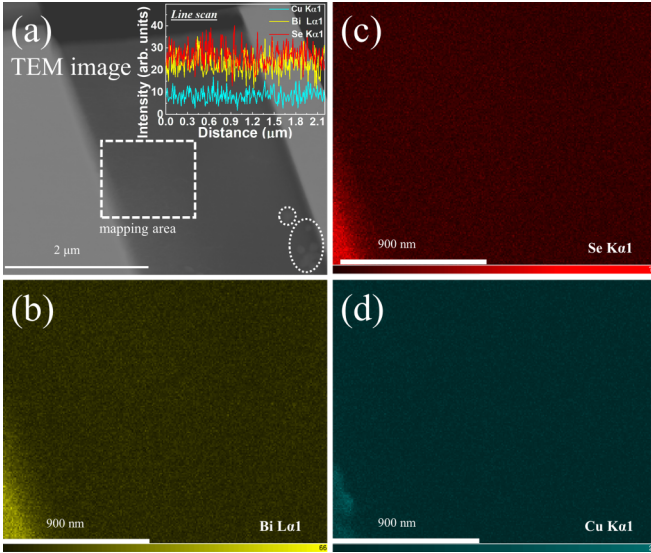
FIG. 5. (a) TEM image of $Cu_{0.1}Bi_2Se_3$; the inset shows the line profile scan results and elemental mapping of the area within the square. The chemical distributions of Bi, Se, and Cu are represented by (b)–(d), respectively.

FIG. 6. Raman spectra of Bi_2Se_3 and $Cu_{0.1}Bi_2Se_3$ at room temperature. Three Raman peaks are found at proximately 75, 133.8, and 176.4 cm^{-1} corresponding to the lattice vibration modes of A_{1g}^1, E_g^2, and A_{1g}^2, respectively. The redshifts represent the out-of-plane direction A_{1g}^1 and A_{1g}^2 modes which are associated with the doping of Cu.

Cui group [14,34], if the atomic ratio of the Cu dopants is high, $x > 0.6$, the Cu atoms will no longer be in the vdW gaps alone, but instead occupy every interstitial location between the quintuple layers, ultimately forming Cu clusters in the vdW gaps. However, with less than 10% copper intercalation of $Cu_{0.1}Bi_2Se_3$, no apparent structural or lattice deformations can be seen in our TEM images. The lattice expansion on the c axis is evidence of the intercalation of Cu in the van der Waals gap, producing a result similar to the XRD refinement discussed earlier. Based on the lattice parameters of XRD refinement, the density of the $Cu_xBi_2Se_3$ crystal was calculated to be 6.68 g/cm^3, which was slightly lower than the 7.51 g/cm^3 of the pristine Bi_2Se_3 crystal (Table I). This was due to the lattice expansion along the c axis that occurred with Cu intercalation.

B. Cu valence: Raman spectra

In order to explore the role and chemical state of copper atoms intercalated between the quintuple layer in our sample, we used Raman spectroscopy to investigate the phonon vibration mode of pristine and optimal $Cu_{0.1}Bi_2Se_3$ single crystal. Figure 6 shows the Raman spectra of pristine Bi_2Se_3 and $Cu_{0.1}Bi_2Se_3$ crystals with $\lambda = 632.8$ nm (He-Ne laser, Renishaw inVia Reflex) excitation at room temperature. The three characteristic main peaks of Bi_2Se_3 at approximately 75, 133.8, and 176.4 cm^{-1} correspond to the vibration modes A_{1g}^1, E_g^2, and A_{1g}^2 as expected. The results agree well with measured results reported by other groups [39–41]. The characteristic Raman active mode will be shifted to higher frequencies when Bi or Se is substituted or by other atoms [42,43]. However, the observed slight redshift indicates the movement of all phonon peaks to lower frequencies in $Cu_{0.1}Bi_2Se_3$ crystal, but there was no drastic shift [41] nor did any new peaks [14] form. Therefore, a slight shift of A_{1g}^1 and A_{1g}^2 implies a weakening of the interactions between the QLs corresponding to the
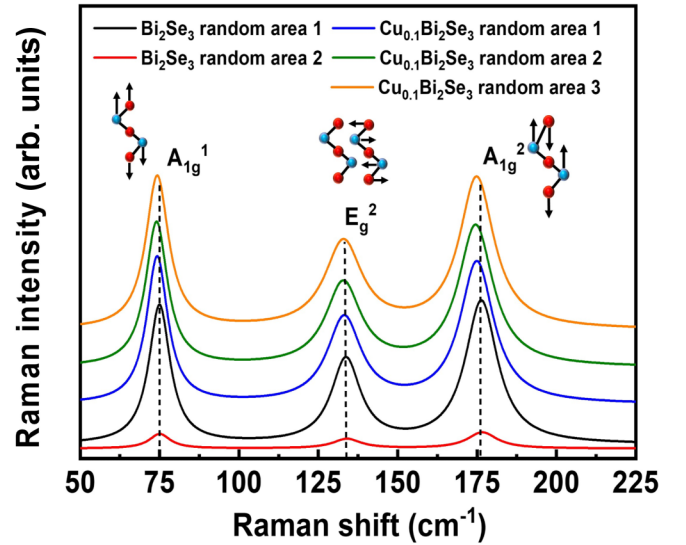
out-of-plane direction, associated with the intercalation of Cu atoms (Table III) [41,42]. The Raman data suggest that Cu atoms occupied the intercalative sites between the QLs; the result agrees with those obtained for the intercalation of Cu in nanowire and thin film [14,43].

C. XPS, AES, and EELS

XPS (Fig. 7, JEOL, JPS-9010MX), AES (Fig. 8, JEOL, JAMP-9500F), and EELS (Fig. 9, Gatan GIF 863 Tridiem) were employed for investigation of the valence of Cu in the $Cu_{0.1}Bi_2Se_3$ crystal. The XPS and AES spectra were obtained by *in situ* ion etching of the uncovered layers at increasing depths. The full range of x-ray photoelectron spectra of $Cu_{0.1}Bi_2Se_3$ is plotted in Fig. 7(a) for qualitative analysis of the elements in the specimen. Four etching processes were performed consecutively with an etching rate of 15 quintuple layers corresponding to 60 QLs per 30 s. The intensity profiles carried out for various depths are listed in Table IV. The characteristic peaks for zero-valence Cu from the top surface to the interior layer were observed at 953.6

TABLE III. Characteristic peak positions of the Bi_2Se_3 reference, Bi_2Se_3, and $Cu_{0.1}Bi_2Se_3$ samples taken from different areas.

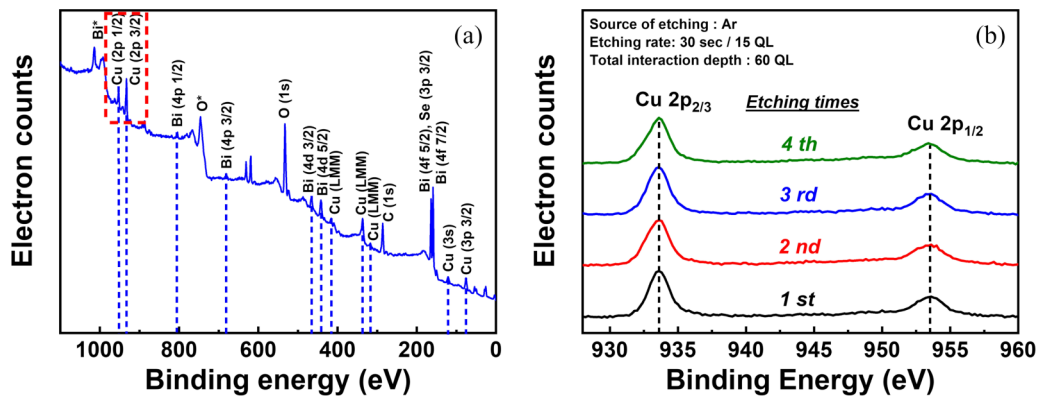| Sample \ Mode	A_{1g}^1 (cm^{-1})	E_g^2 (cm^{-1})	A_{1g}^2 (cm^{-1})
Bi_2Se_3 [44,45]	73	133	175
Bi_2Se_3 (area 1)	75.03	134.11	176.56
Bi_2Se_3 (area 2)	75.00	133.65	176.31
$Cu_{0.1}Bi_2Se_3$ (area 1)	74.35	133.12	174.92
$Cu_{0.1}Bi_2Se_3$ (area 2)	74.10	132.87	174.42
$Cu_{0.1}Bi_2Se_3$ (area 3)	74.35	132.87	174.92

FIG. 7. (a) Full range of x-ray photoelectron spectra of $Cu_{0.1}Bi_2Se_3$; (b) selected XPS spectra nearby the Cu $2p$ orbitals for four depths showing only two Cu zero-valence characteristic peaks at 953.6 and 933.6 eV for Cu $2p_{1/2}$ and Cu $2p_{3/2}$, respectively.
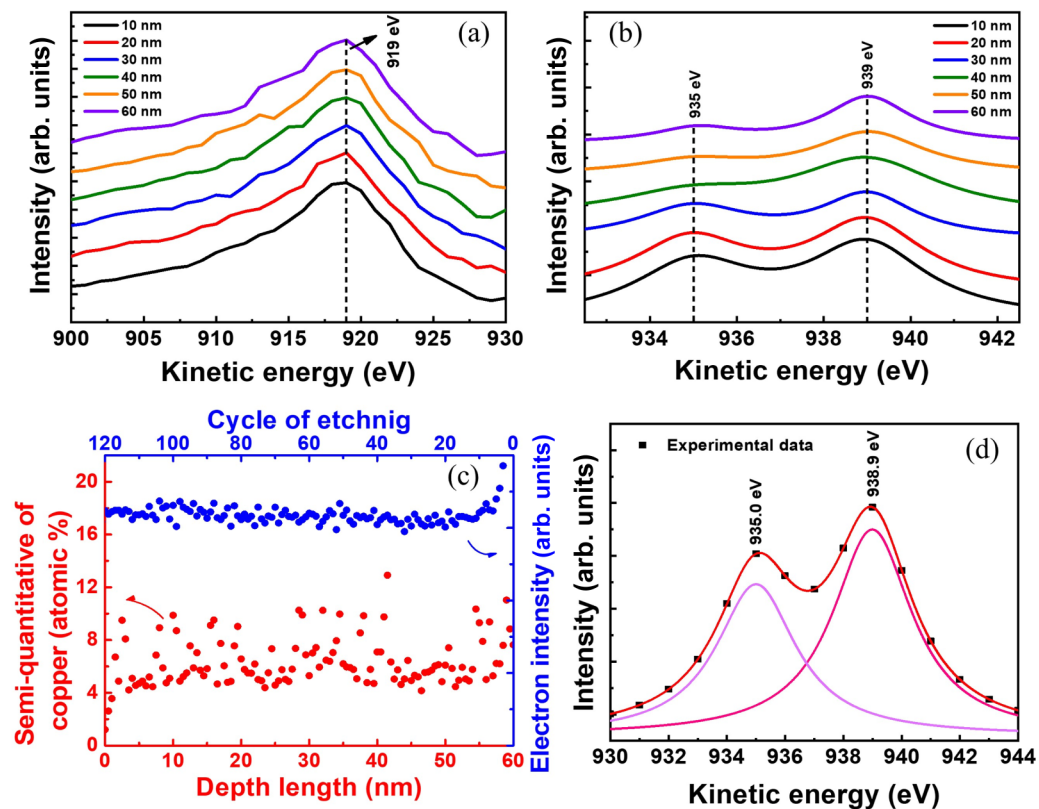

FIG. 8. (a), (b) Cu LVV Auger electron spectra of $Cu_{0.1}Bi_2Se_3$; (c) depth dependence of the electron intensity and semiquantitative percentage of Cu represented by red and blue spots, respectively; (d) quantitative analysis with multipeak fitting at consecutive peaks (935 and 939 eV) from the raw AES data.

TABLE IV. Position of the characteristic peaks of Cu $2p$ orbitals as a function of the interaction depth. The reaction depth is proportional to the etching time.

Etching steps (Ar ion)	Duration (s) Etching rate: 30 s /15 QL	Characteristic peak Cu $2p_{2/3}$ (eV)	Characteristic peak Cu $2p_{1/3}$ (eV)
First	30 (15 QL)	933.6	953.6
Second	30 (30 QL)	933.6	953.6
Third	30 (45 QL)	933.6	953.6
Fourth	30 (60 QL)	933.6	953.4
Reference [34]		934.0	954.0
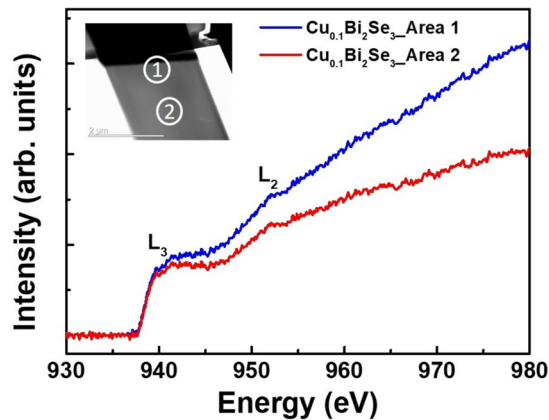
FIG. 9. Upper inset: TEM image of the $Cu_{0.1}Bi_2Se_3$. The EELS results for $Cu_{0.1}Bi_2Se_3$ detected in area 1 and area 2 correspond to the blue and red curves, respectively. The steplike behavior at L_2 and L_3 is consistent with previous reports [14,34], indicating that it arises from the zero-valence Cu.

and 933.6 eV for Cu $2p_{1/2}$ and Cu $2p_{3/2}$, respectively. There are no visible satellite peaks between the two main peaks [Fig. 7(b)]. Thus, the XPS spectra clearly rule out the Cu^{2+} state in our specimen but there is need for further analysis to identify the Cu^0 and Cu^{+1} state. It can be seen that the position of all characteristic peaks of zero-valence Cu remain the same with the increase in depth [Fig. 7(b)]. Meanwhile, the normalized XPS data show the zero-valence Cu to be uniformly and homogeneously distributed, a result similar to that obtained in the study of Cu^{2+} and Cu^+ compounds [46–48].

AES was applied to further study the electronic states of Cu^0 and Cu^{+1}. The depth profiles and characteristic peaks of 919, 935, and 939 eV for Cu plotted in Figs. 8(a) and 8(b) are similar to those for metallic Cu as previously reported [49]. The relative semiquantitative and electron intensity as shown in Fig. 8(c) indicate a uniform and homogeneous distribution of zero-valence copper in the top surface and inner layers. Quantitative analysis was performed by multipeak fitting to obtain a reasonable explanation of the noticeable broad peak (at 919 eV) and consecutive peak (at 935 and 939 eV) in the spectra. However, the fitting could not be achieved for the broadening peak at 919 eV due to there being much fewer Cu atoms (∼2 at. %) in the specimen. It was not easy to separate each peak around the energy window of 900–930 eV compared to the pure Cu sample. Therefore, the two peaks around 935 and 938.9 eV may play a role as key characteristic peaks for identifying the presence of zero-valence Cu, as plotted in Fig. 8(d). The AES results give more evidence of the proposition of the Cu atoms being zero-valence metallic copper.

EELS is a powerful technique for identifying the chemical state of a transition metal, such as the L_3/L_2 ratio [50]. Therefore, the EELS fine structure is also used to determine the chemical state of the $Cu_{0.1}Bi_2Se_3$. The blue and red solid lines in Fig. 9 correspond to two different detected areas, both of which exhibit the typical steplike behavior in the characteristic spectra noted by Zhang [14] and Koski [38] *et al.* rather than

the peaklike feature [52]. The EELS results of $Cu_{0.1}Bi_2Se_3$ clearly differ from those of nonzero-valent Cu compounds, indicating no nonzero oxidation states in $Cu_{0.1}Bi_2Se_3$. The above XPS, AES, and EELS results for $Cu_xBi_2Se_3$ suggest that the Cu was zero valence. Indeed, as suggested [53] by Ribak *et al.*, the intercalation of Cu created stress and increased the population of electrons in the conduction band.

D. Superconductivity in electrical transport and magnetization

Due to the native Se vacancy (V_{Se}) and Bi antisite (Bi_{Se}) defects in the as-grown material, bulk bismuth selenides turned out to be an intrinsic *n*-type material, with site occupation playing an important role in the superconductivity of this system [11,12]. Analysis of the temperature and magnetic field dependence of the electrical conductivity of $Cu_{0.1}Bi_2Se_3$ in the *a-b* plane was carried out by PPMS (PPMS®, Quantum Design) with the four-probe method. Figure 10(a) shows the normalized temperature dependence of the resistance for Bi_2Se_3 and $Cu_{0.1}Bi_2Se_3$ at $T = 1.8$ to 300 K. In contrast to Bi_2Se_3, a superconducting transition arises in $Cu_{0.1}Bi_2Se_3$. The offset and onset temperatures are determined to be 3 and 3.4 K, respectively [see the inset of Fig. 10(a)]. The minor difference in the resistivity above the transition temperature from that of Bi_2Se_3 supports the hypothesis that the Cu atoms intercalated in the van der Waals gaps are electronically neutral. The temperature dependence of the magnetoresistance of $Cu_{0.1}Bi_2Se_3$ for $T = 1.8$ to 4 K is plotted in Fig. 10(b). A typical symmetric resistance behavior at all temperatures is exhibited. The upper critical fields (H_{C2}) increase with decreasing temperature as shown in the inset to Fig. 10(b) (determined by a 50% resistance drop of the normal state [54]). The black solid line stands for the field-dependent resistance behavior at 1.8 K; the H_{C2} was determined to be approximately 0.9 T.

In order to obtain the best superconducting specimen with the largest diamagnetic shielding fraction, in addition to the $Cu_xBi_2Se_3$ crystals studied above, which were fabricated by the Bridgman method (BM) followed by EC deposition (named BM+EC), two other sample fabrication methods were employed to synthesize $Cu_xBi_2Se_3$: (I) mixed furnace melting (MFM): $Cu_xBi_2Se_3$ was directly fabricated by melting elements of copper, bismuth, and selenium with the appropriate stoichiometric ratio in a furnace; (II) FM+EC method: starting from a Bi_2Se_3 ingot, followed by electrochemical deposition for Cu intercalation.

The temperature dependence of the magnetic shielding fraction of $Cu_xBi_2Se_3$ fabricated by the three different methods is measured by MPMS (MPMS®XL, Quantum design); see Fig. 11(a). The SC shielding fraction f_s is defined by $f_s = 4\pi\rho\chi_m \times 100\%$, where ρ and χ_m are the mass density and magnetic susceptibility, respectively. The volume of the sample was considered for estimation of the shielding fraction. Here, we used a planar sample and applied the magnetic field parallel to the plane; the demagnetization correction should be negligible. The shielding fractions of specimens of MFM and FM+EC were 35% and 58%, respectively, while the BM+EC specimen showed the largest shielding fraction of 84%. Moreover, the BM+EC specimen also exhibited the highest-onset superconducting temperature of 3.4 K
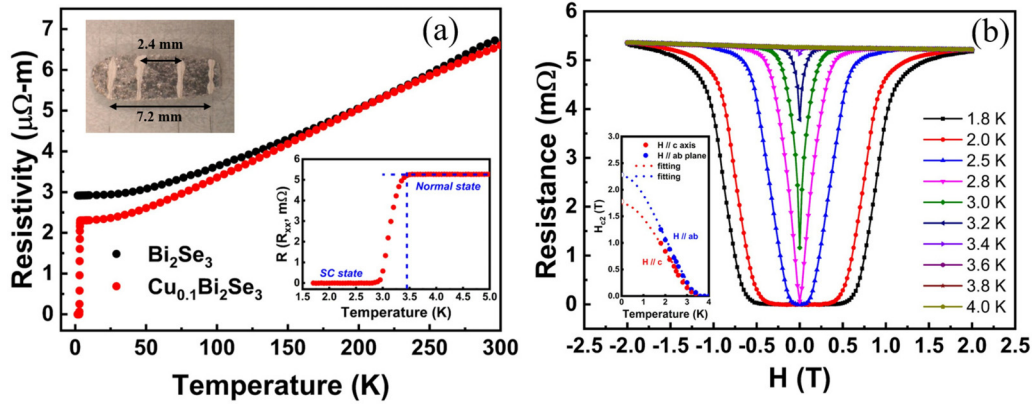
FIG. 10. (a) Temperature dependence of the resistance for Bi_2Se_3 and $Cu_{0.1}Bi_2Se_3$. A sharp superconducting transition at 3.4 K is shown in the bottom right inset. The upper inset shows the application of electrical current in the *ab* plane; probes were connected by silver paste. (b) The magnetic dependence of the resistance of $Cu_{0.1}Bi_2Se_3$ at various temperatures. The left inset indicates the critical magnetic field values for $H//ab$ and $H \perp ab$, which allow for the extrapolation of zero-temperature values.

compared to 3.3 and 3.0 K for the MFM and FM+EC specimens, respectively. The much broader SC transitions observed in both the MFM and FM+EC specimens were associated to the nonuniformity of Cu intercalation or the absence of a continuous superconducting path [11,12,40]. The temperature dependence of the shielding fractions for specimens with different Cu levels (BM+EC) is shown in Fig. 11(b). Based on the maximum f_s and T_c [see the inset to Fig. 11(b)], the optimal Cu doping level of $Cu_xBi_2Se_3$ is about $x = 0.1$, which is similar to the reported values [12].

The specific heat data confirm the superconductivity of the $Cu_{0.1}Bi_2Se_3$ crystal. The temperature dependence of C_P/T in 0 and 2 T applied along the *c* axis is plotted in Fig. 12(a). The electronic contribution C_{el} is shown in Fig. 12(b) as C_{el}/T vs T for SC state ($H = 0$ T). C_{el} is obtained by subtracting the phononic contribution evaluated from the specific heat at 2 T excluding the electronic part γT [the inset of Fig. 12(a)], revealing the sharp specific heat of the superconductivity at $T_c = 3.2$ K. The absence of the Schottky anomaly in the high magnetic field suggested that there was no local moment possibly associated with the Cu^{+2} ions. The electronic specific heat data were fit to a modified Bardeen–Cooper–Schrieffer

(BCS) model (α model) to derive $\alpha = 1.9$ which was larger than the $\alpha = 1.764$ of a typical BCS superconductor. The results suggest that $Cu_{0.1}Bi_2Se_3$ may be an unconventional superconductor.

To evaluate the volume fraction of superconductivity, the α model [55] was employed as described in Eqs. (1)–(3):

$$S_{es}(t)/\gamma T_c = -(3\alpha/\pi^2)\int_0^\infty dx[f_x ln f_x + (1-f_x)ln(1-f_x)],$$

(1)

where

$$f_x = [\exp \alpha t^{-1}(x^2 + \delta^2)^{1/2} + 1]^{-1};$$

(2)

$$C_{es}(t)/\gamma T_c = t(d/dt)(S_{es}/\gamma T_c),$$

(3)

where $S_{es}(t)$ is the entropy of electrons, $\alpha \equiv \Delta(0)/k_B T_c$ is the strength of the coupling, $t \equiv T/T_c$ is the reduced temperature, and $\delta(T) \equiv \Delta(T)/\Delta(0)$ is the reduced energy gap, respectively.
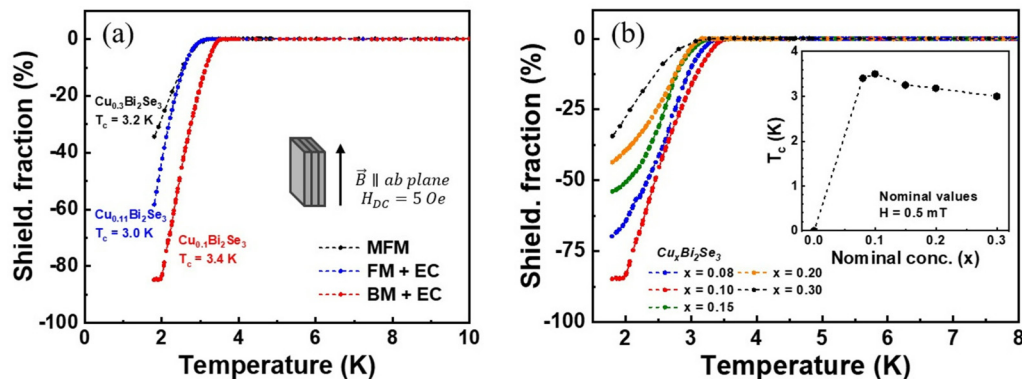

FIG. 11. (a) Temperature dependence of the shielding fraction of $Cu_xBi_2Se_3$ synthesized with different methods in $B = 0.5$ mT$//ab$; (b) shielding fraction for various Cu concentrations. Inset to (b) shows the Cu content dependence of the critical temperature of the superconductivity.
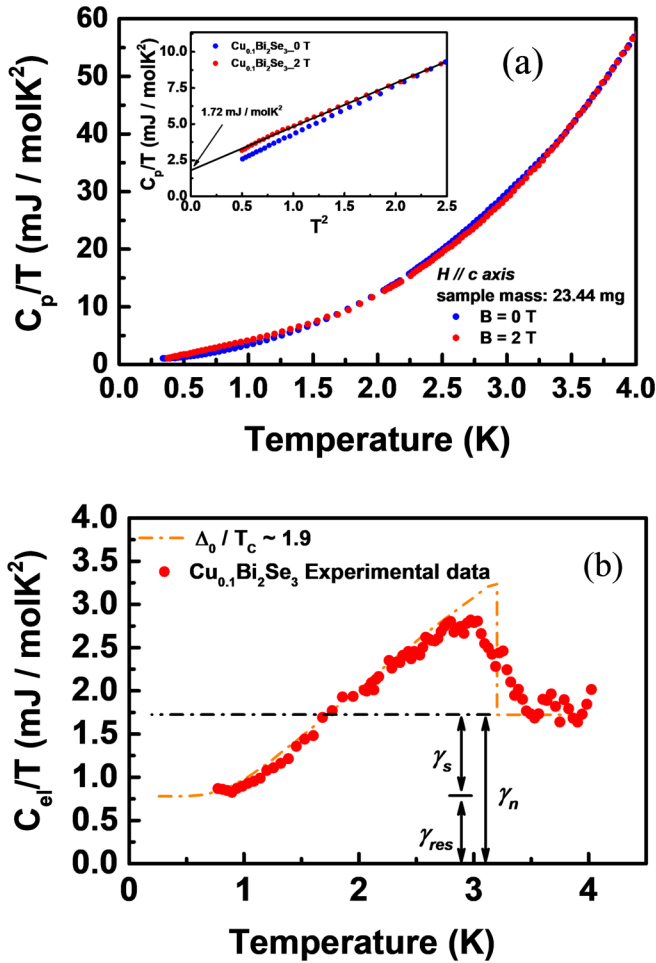
FIG. 12. (a) The temperature dependence of C_p is shown as C_p/T vs T for the SC state at zero field and the normal state is achieved by applying $H = 2\,T//c$ axis for $Cu_{0.1}Bi_2Se_3$. Inset: C_P/T vs T^2 measured in 0 and 2 T. (b) The electronic contribution of the specific heat (solid red dot) and 80% of the calculated α model (orange line). The horizontal dash-dotted line denotes the value of γ_n, and it is composed of γ_s and γ_{res}.

Two methods were used to calculate the superconducting volume fraction; one is fitting the superconducting transition profile by the α model, and the other is using the ratio of γ_s/γ_n [56]. By fitting the superconducting transition profile to the α model, the superconducting volume fraction was estimated to be ~80%, shown in Fig. 12(b), whereas the superconducting volume fraction calculated by γ_s/γ_n was 53% with $\gamma_s = 0.92\,\mathrm{mJ/mol\,K^2}$ and $\gamma_n = 1.72\,\mathrm{mJ/mol\,K^2}$,

respectively. Since γ_{res} may include the contribution of impurities, thus γ_n may be overestimated, and the ratio of $\gamma_s/\gamma_n = 53\%$ would be the lowest limit of the superconducting volume fraction. Due to the uncertainty from γ_n, the superconducting volume fraction estimated from specific heat data is suggested to be between 53% and 80%.

III. CONCLUSION

High-quality Bi_2Se_3 and superconducting $Cu_xBi_2Se_3$ crystals have been successfully synthesized using the Bridgman method and EC Cu deposition. XRD analysis shows lattice expansion of the c axis which suggests that copper was intercalated into the vdW gaps. The HRTEM images and SAED patterns also reveal that the intercalation of Cu does not cause crystal distortion or lattice deformation from the nominal space group. The SEM images reveal the aggregation of some copper and the formation of clusters which coexist with the uniformly distributed copper in the vdW gaps. The Raman shift data are in good agreement with Cu intercalation in the vdW gaps. The normalized XPS data show the uniform and homogeneous distribution of Cu in the specimen and the AES measurements supply evidence of the zero valence of the copper atoms. The EELS measurements of $Cu_{0.1}Bi_2Se_3$ are clearly different from those of nonzero-valent copper compounds, indicating that there are no nonzero oxidation states in the $Cu_{0.1}Bi_2Se_3$. The temperature dependence of the resistance, magnetic susceptibility, and specific heat confirms bulk superconductivity in our $Cu_xBi_2Se_3$ crystals. Superconducting $Cu_{0.1}Bi_2Se_3$ with a shielding fraction f_s up to 84% was achieved, indicating the high quality of the single crystal produced by superconducting $Cu_{0.1}Bi_2Se_3$ growth through the Bridgman method followed by the intercalation of Cu using electrochemical deposition. This study gives more detailed evidence of the microstructure and spectroscopic results identifying the zero valence of the intercalated Cu throughout single-crystal $Cu_xBi_2Se_3$. The confirmation of zero-valence Cu implies that the formation of superconducting quasiparticles is more likely associated with the topology of the copper distribution and or c-axis lattice strain than the modification of the band structure by electronic charge transfer.

[1] L. Fu and C. L. Kane, Superconducting Proximity Effect and Majorana Fermions at the Surface of a Topological Insulator, Phys. Rev. Lett. **100**, 096407 (2008).

[2] L. Fu and C. L. Kane, Topological insulators with inversion symmetry, Phys. Rev. B **76**, 045302 (2007).

[3] D. Hsieh, D. Qian, L. Wray, Y. Xia, Y. S. Hor, R. J. Cava, and M. Z. Hasan, A topological Dirac insulator in a quantum spin Hall phase, Nature **452**, 970 (2008).

[4] H. Zhang, C. X. Liu, X. L. Qi, X. Dai, Z. Fang, and S. C. Zhang, Topological insulators in Bi_2Se_3, Bi_2Te_3 and Sb_2Te_3 with a single Dirac cone on the surface, Nat. Phys. **5**, 438 (2009).

[5] L. A. Wray, S. Xu, Y. Xia, D. Qian, A. V. Fedorov, H. Lin, A. Bansil, L. Fu, Y. S. Hor, R. J. Cava, and M. Z. Hasan, Spin-orbital ground states of superconducting doped topological insulators: A Majorana platform, Phys. Rev. B **83**, 224516 (2011).

[6] L. Fu and E. Berg, Odd-Parity Topological Superconductors: Theory and Application to $Cu_xBi_2Se_3$, Phys. Rev. Lett. **105**, 097001 (2010).

[7] K. Matano, M. Kriener, K. Segawa, Y. Ando, and G. Q. Zheng, Spin-rotation symmetry breaking in the superconducting state of $Cu_xBi_2Se_3$, Nat. Phys. **12**, 852 (2016).

[8] S. Yonezawa, S. Tajiri, S. Nakata, Y. Nagai, Z. W. Wang, K. Segawa, Y. Ando, and Y. Maeno, Thermodynamic evidence for nematic superconductivity in $Cu_xBi_2Se_3$, Nat. Phys. **13**, 123 (2017).

[9] J. A. Schneeloch, R. D. Zhong, Z. J. Xu, G. D. Gu, and J. M. Tranquada, Dependence of superconductivity in $Cu_xBi_2Se_3$ on quenching conditions, Phys. Rev. B **91**, 144506 (2015).

[10] M. Wang, Y. R. Song, L. X. You, Z. J. Li, B. Gao, X. M. Xie, and M. H. Jiang, A combined method for synthesis of superconducting Cu doped Bi_2Se_3, Sci. Rep. **6**, 22713 (2016).

[11] Y. S. Hor, A. J. Williams, J. G. Checkelsky, P. Roushan, J. Seo, Q. Xu, H. W. Zandbergen, A. Yazdani, N. P. Ong, and R. J. Cava, Superconductivity in $Cu_xBi_2Se_3$ and its Implications for Pairing in the Undoped Topological Insulator, Phys. Rev. Lett. **104**, 057001 (2010).

[12] M. Kriener, K. Segawa, Z. Ren, S. Sasaki, S. Wada, S. Kuwabata, and Y. Ando, Electrochemical synthesis and superconducting phase diagram of $Cu_xBi_2Se_3$, Phys. Rev. B **84**, 054513 (2011).

[13] S. Sasaki, M. Kriener, K. Segawa, K. Yada, Y. Tanaka, M. Sato, and Y. Ando, Topological Superconductivity in $Cu_xBi_2Se_3$, Phys. Rev. Lett. **107**, 217001 (2011).

[14] J. S. Zhang, J. Sun, Y. B. Li, F. F. Shi, and Y. Cui, Electrochemical control of copper intercalation into nanoscale Bi_2Se_3, Nano Lett. **17**, 1741 (2017).

[15] R. D. Shannon, Revised effective ionic radii and systematic studies of interatomic distances in halides and chaleogenides, Acta Crystallogr. **A32**, 751 (1976).

[16] Y. H. Choi, N. H. Jo, K. J. Lee, H. W. Lee, Y. H. Jo, J. Kajino, T. Takabatake, K. T. Ko, J. H. Park, and M. H. Jung, Simple tuning of carrier type in topological insulator Bi_2Se_3 by Mn doping, Appl. Phys. Lett. **101**, 152103 (2012).

[17] Z. W. Wang, A. A. Taskin, T. Frölich, M. Braden, and Y. Ando, Superconductivity in $Tl_{0.6}Bi_2Te_3$ Derived from a Topological Insulator, Chem. Mater. **28**, 779 (2016).

[18] T. Asaba, B. J. Lawson, C. Tinsman, L. Chen, P. Corbae, G. Li, Y. Qiu, Y. S. Hor, L. Fu, and L. Li, Rotational Symmetry Breaking in a Trigonal Superconductor Nb-doped Bi_2Se_3, Phys. Rev. X **7**, 011009 (2017).

[19] M. P. Smylie, K. Willa, H. Claus, A. Snezhko, I. Martin, W.-K. Kwok, Y. Qiu, Y. S. Hor, E. Bokari, P. Niraula, A. Kayani, V. Mishra, and U. Welp, Robust odd-parity superconductivity in the doped topological insulator $Nb_xBi_2Se_3$, Phys. Rev. B **96**, 115145 (2017).

[20] Y. S. Hor, A. Richardella, P. Roushan, Y. Xia, J. G. Checkelsky, A. Yazdani, M. Z. Hasan, N. P. Ong, and R. J. Cava, p-type Bi_2Se_3 for topological insulator and low-temperature thermoelectric applications, Phys. Rev. B **79**, 195208 (2009).

[21] Z. Ren, A. A. Taskin, S. Sasaki, K. Segawa, and Y. Ando, Observations of two-dimensional quantum oscillations and ambipolar transport in the topological insulator Bi_2Se_3 achieved by Cd doping, Phys. Rev. B **84**, 075316 (2011).

[22] Shruti, V. K. Maurya, P. Neha, P. Srivastava, and S. Patnaik, Superconductivity by Sr intercalation in the layered topological insulator Bi_2Se_3, Phys. Rev. B **92**, 020506(R) (2015).

[23] C. Q. Han, H. Li, W. J. Chen, F. F. Zhu, M. Y. Yao, Z. J. Li, M. Wang, B. F. Gao, D. D. Guan, C. H. Liu, C. L. Gao, D. Qian, and J. F. Jia, Electronic structure of a superconducting topological insulator Sr-doped Bi_2Se_3, Appl. Phys. Lett. **107**, 171602 (2015).

[24] Y. H. Zhou, X. L. Chen, R. R. Zhang, J. F. Shao, X. F. Wang, C. An, Y. Zhou, C. Y. Park, W. Tong, L. Pi, Z. R. Yang, C. J. Zhang, and Y. H. Zhang, Pressure-induced reemergence of superconductivity in topological insulator $Sr_{0.065}Bi_2Se_3$, Phys. Rev. B **93**, 144514 (2016).

[25] K. Willa, R. Willa, K. W. Song, G. D. Gu, John A. Schneeloch, R. D. Zhong, Alexei E. Koshelev, W. K. Kwok, and U. Welp, Nanocalorimetric evidence for nematic superconductivity in the doped topological insulator $Sr_{0.1}Bi_2Se_3$, Phys. Rev. B **98**, 184509 (2018).

[26] M. P. Smylie, K. Willa, H. Claus, A. E. Koshelev, K. W. Song, W. K. Kwok, Z. Islam, G. D. Gu, J. A. Schneeloch, R. D. Zhong, and U. Welp, Superconducting and normal-state anisotropy of the doped topological insulator $Sr_{0.1}Bi_2Se_3$, Sci. Rep. **8**, 7666 (2018).

[27] G. Du, Y. F. Li, J. Schneeloch, R. D. Zhong, G. D. Gu, H. Yang, H. Lin, and H. H. Wen, Superconductivity with two-fold symmetry in topological superconductor $Sr_xBi_2Se_3$, Sci. China Phys. Mech. Astron. **60**, 037411 (2017).

[28] L. Hao and C. S. Ting, Nematic superconductivity in $Cu_xBi_2Se_3$: Surface Andreev bound states, Phys. Rev. B **96**, 144512 (2017).

[29] F. C. Wu and I. Martin, Nematic and chiral superconductivity induced by odd-parity fluctuations, Phys. Rev. B **96**, 144504 (2017).

[30] M. T. Li, Y F Fang, J. C. Zhang, H. M. Yi, X. J. Zhou, and C. T. Lin, Magnetotransport study of topological superconductor $Cu_{0.10}Bi_2Se_3$ single crystal, J. Phys.: Condens. Matter **30**, 125702 (2018).

[31] R. W. G. Wyckoff, *Crystal Structures* (John Wiley & Sons, New York, London, 1964).

[32] H. Okamoto, The Bi-Se (bismuth-selenium) system, J. Phase Equilib. **15**, 195 (1994).

[33] X. Chen, H. D. Zhou, A. Kiswandhi, I. Miotkowski, Y. P. Chen, P. A. Sharma, A. L. Lima Sharma, M. A. Hekmaty, D. Smirnov, and Z. Jiang, Thermal expansion coefficients of Bi_2Se_3 and Sb_2Te_3 crystals from 10 K to 270 K, Appl. Phys. Lett. **99**, 261912 (2011).

[34] K. J. Koski, J. J. Cha, B. W. Reed, C. D. Wessells, D. Kong, and Yi Cui, High-density chemical intercalation of zero-valent copper into Bi_2Se_3 nanoribbons, J. Am. Chem. Soc. **134**, 7584 (2012).

[35] F. T. Huang, M. W. Chu, H. H. Kung, W. L. Lee, R. Sankar, S. C. Liou, K. K. Wu, Y. K. Kuo, and F. C. Chou, Nonstoichiometric doping and Bi antisite defect in single crystal Bi_2Se_3, Phys. Rev. B **86**, 081104(R) (2012).

[36] *Progress in Intercalation Research*, edited by W. Müller-Warmuth and R. Schöllhorn (Kluwer, Dordrecht, Netherlands, 1994).

[37] *Intercalation in Layered Materials*, edited by M. S. Dresselhaus, NATO Science Series B (Plenum Press, New York, 1987), Vol. 148.

[38] *Intercalated Layered Materials*, edited by F. Lévy (Reidel, Dordrecht, Netherlands, 1979).

[39] J. Zhang, Z. P. Peng, A. Soni, Y. Y. Zhao, Y. Xiong, B. Peng, J. B. Wang, M. S. Dresselhaus, and Q. H. Xiong, Raman spectroscopy of few-quintuple layer topological insulator Bi_2Se_3 nanoplatelets, Nano Lett. **11**, 2407 (2011).

[40] K. M. F. Shahil, M. Z. Hossain, V. Goyal, and A. A. Balandin, Micro-Raman spectroscopy of mechanically exfoliated few-quintuple layers of Bi_2Te_3, Bi_2Se_3, and Sb_2Te_3 materials, J. Appl. Phys. **111**, 054305 (2012).

[41] W. Richter, H. Köhler, and C. R. Becker, A Raman and far-infrared investigation of phonons in the rhombohedral V2-V13 compounds, Phys. Status Solidi B **84**, 619 (1977).

[42] H. J. Chen, K. H. Wu, C. W. Luo, T. M. Uen, J. Y. Juang, J. Y. Lin, T. Kobayashi, H. D. Yang, R. Sankar, F. C. Chou, H. Berger, and J. M. Liu, Phonon dynamics in $Cu_xBi_2Se_3$ ($x =$ 0, 0.1, 0.125) and Bi_2Se_2 crystals studied using femtosecond spectroscopy, Appl. Phys. Lett. **101**, 121912 (2012).

[43] M. Z. Li, Z. H. Wang, L. Yang, D. Li, Q. R. Yao, G. H. Rao, X. P. A. Gao, and Z. D. Zhang, Electron delocalization and relaxation behavior in Cu-doped Bi_2Se_3 films, Phys. Rev. B **96**, 075152 (2017).

[44] V. Gnezdilov, Yu. G. Pashkevich, H. Berger, E. Pomjakushina, K. Conder, and P. Lemmens, Helical fluctuations in the Raman response of the topological insulator Bi_2Se_3, Phys. Rev. B **84**, 195118 (2011).

[45] I. Boulares, G. Shi, E. Kioupakis, P. Lošťák, C. Uher, and R. Merlin, Surface phonons in the topological insulators Bi_2Se_3 and Bi_2Te_3, Solid State Commun. **271**, 1 (2018).

[46] G. Panzner, B. Egert, and H. P. Schmidt, The stability of CuO and Cu_2O surfaces during argon sputtering studied by XPS and AES, Surf. Sci. **151**, 400 (1985).

[47] S. Colin, E. Beche, R. Berjoan, H. Jolibois, and A. Chambaudet, An XPS and AES study of the free corrosion of Cu-, Ni- and Zn-based alloys in synthetic sweat, Corros. Sci. **41**, 1051 (1999).

[48] S. Hüfner, *Photoelectron Spectroscopy Principles and Applications* (Springer, New York, 2003), Chap. 5.9, p. 315.

[49] T. S. Niedrig, T. Neisius, I. Böttger, E. Kitzelmann, G. Weinberg, D. Demuth, and R. Schlögl, Copper (sub)oxide formation: A surface sensitive characterization of model catalysts, Phys. Chem. Chem. Phys. **2**, 2407 (2000).

[50] R. F. Egerton, Electron energy-loss spectroscopy in the TEM, Rep. Prog. Phys. **72**, 016502 (2009).

[51] S. Nakajima, The crystal structure of $Bi_2Te_{3-x}Se_x$, J. Phys. Chem. Solids **24**, 479 (1963).

[52] L. Laffont, M. Y. Wu, F. Chevallier, P. Poizot, M. Morcrette, and J. M. Tarascon, High resolution EELS of Cu–V oxides: Application to batteries materials, Micron **37**, 459 (2006).

[53] A. Ribak, K. B. Chashka, E. Lahoud, M. Naamneh, S. Rinott, Y. Ein-Eli, N. C. Plumb, M. Shi, E. Rienks, and A. Kanigel, Internal pressure in superconducting Cu-intercalated Bi_2Se_3, Phys. Rev. B **93**, 064505 (2016).

[54] C. C. Almasan, M. C. de Andrade, Y. Dalichaouch, J. J. Neumeier, C. L. Seaman, M. B. Maple, R. P. Guertin, M. V. Kuric, and J. C. Garland, Evidence for Scaling Invariance and Universality of the Irreversibility Line of High Temperature Superconductors, Phys. Rev. Lett. **69**, 3812 (1992).

[55] H. Padamsee, J. E. Neighbor, and C. A. Shiffman, Quasiparticle phenomenology for thermodynamics of strong-coupling superconductors, J. Low Temp. Phys. **12**, 387 (1973).

[56] M. Kriener, K. Segawa, Z. Ren, S. Sasaki, and Y. Ando, Bulk Superconducting Phase with a Full Energy Gap in the Doped Topological Insulator $Cu_xBi_2Se_3$, Phys. Rev. Lett. **106**, 127004 (2011).